Advancing Scanning Probe Microscopy Simulations: A Decade of Development in Probe-Particle Models

Niko Oinonen[a,b,*], Aliaksandr V. Yakutovich[c,d,*], Aurelio Gallardo[e], Martin Ondráček[f], Prokop Hapala[f,**], Ondřej Krejčí[a,**]

[a]*Aalto University, Department of Applied Physics, P.O. Box 11000 (Otakaari 1B), AALTO, FI-00076, Finland*
[b]*Nanolayers Research Computing Ltd, 51 New Way Road, London, NW9 6PL, United Kingdom*
[c]*nanotech@surfaces laboratory, Swiss Federal Laboratories for Materials Science and Technology (Empa), Überlandstrasse 129, Dübendorf, CH-8600, Switzerland*
[d]*National Centre for Computational Design and Discovery of Novel Materials (MARVEL), École Polytechnique Fédérale de Lausanne, Lausanne, CH-1015, Switzerland*
[e]*IMDEA Nanoscience Institute, C/ Faraday 9, Campus de Cantoblanco, Madrid, 28049, , Spain*
[f]*FZU - Institute of Physics of the Czech Academy of Sciences, Na Slovance 1999/2, Prague 8, 182 00, , Czech Republic*

Abstract

The probe-particle model is an open-source package designed for simulation of scanning probe microscopy experiments, employing non-reactive, flexible tip apices (e.g., carbon monoxide, xenon, or hydrogen molecules) to achieve *sub-molecular resolution*. This abstract introduces the latest version of the probe-particle model, highlighting substantial advancements in accuracy, computational performance, and user-friendliness over previous versions. To demonstrate this we provide a comprehensive review of theories for simulating non-contact Atomic Force Microscopy (nc-AFM), spanning from the simple Lennard-Jones potential to the latest *full density-based model*. Implementation of these theories are systematically compared against *ab initio* calculated reference, showcasing their respective merits. All parts of the probe-particle model have undergone acceleration by 1-2 orders of magnitude through parallelization by OpenMP on CPU and OpenCL on GPU. The updated package includes an interactive graphical user interface (GUI) and seamless integration into the Python ecosystem via pip, facilitating advanced scripting and interoperability with other software. This adaptability positions the probe-particle model as an ideal tool for high-throughput applications, including the training of machine learning models for the automatic recovery of atomic structures from nc-AFM measurements. We envision significant potential for this application in future single-molecule analysis, synthesis, and advancements of surface science in general. Additionally, we discuss simulations of other *sub-molecular* scanning-probe imaging techniques, such as bond-resolved scanning tunneling microscopy and kelvin probe force microscopy, all built on the robust foundation of the probe-particle model. Altogether this demonstrates the broad impact of the model across diverse domains of surface science and molecular chemistry.

Keywords: Scanning Probe Microscopy, Atomic Force Microscopy Simulations, Bond-Resolved Atomic Force Microscopy

1. Introduction

The first Scanning Tunneling Microscopy (STM) and Atomic Force Microscopy (AFM) instruments, developed in 1981 [1] and 1986 [2], respectively, showcased the ability to visualize individual atoms of inorganic substrates. It took, however, another two decades of scanning probe microscopy (SPM) development to distinguish individual atoms inside organic molecules separated by a distance less than 1.5 Å, achieving *sub-molecular resolution*. This was accomplished by passivating the apex of the metallic tip with an inert molecule (carbon monoxide, hydrogen) or atom (Xe) [3, 4]. Due to their low reactivity, these tip apices reduce the possibility of damaging or manipulating the sample. Furthermore, the molecules are rather loosely attached to metallic tips, which makes them flexible. As a result, high-resolution scanning probe microscopy (HR-SPM) techniques need to function at low temperatures ($\leq$ 10 K) to minimize thermal motion and prevent the passivating molecule or atom from desorbing from the tip.

The flexibility of the molecule attached to the tip allows it to deflect during the interaction with the sample. The tip apex deflection produces image distortions, which manifest themselves as either sharp lines at the ridges of the potential energy surface resembling bonds in HR-AFM [5] or a discontinuous contrast in the HR-STM images [5, 6]. A similar effect can be also found in Inelastic Electron Tunnelling Spectroscopy (IETS) [7].

The SPM has become a powerful tool for the chemical analysis and synthesis of individual organic molecules due to its ability to distinguish atoms at close distances, manipulate them, as well as to differentiate bond types. For instance, the HR-AFM with CO-decorated tip is sensitive to a bond order in aromatic systems [8], free electron pairs in highly electronegative atoms [9], the orbital configuration of transition metals in organometallic compounds [10].

The capabilities of SPM techniques made them invaluable tools not only in fundamental research (e.g. for the develop-

*Authors contributed equally
**Corresponding authors
Email adresses: hapala@fzu.cz, ondrej.krejci@aalto.fi

ment of futuristic molecular nanotechnology [11] and new materials) but also in practical industrial applications. Currently, SPM helps in deciphering the chemical structures of individual molecules within complex mixtures, such as crude oil or decomposing and carbonized organic materials in the depth of oceans [12–14]. HR-SPM has been also extremely useful for the recognition of complex materials and their surfaces such as calcium carbonate and fluoride [15, 16], showing the HR-SPM general applicability over several scientific disciplines.

Due to single molecule resolution, HR-SPM techniques allows avoiding preparation of pure substances in macroscopic quantities which is required by other techniques for structural analysis such as X-ray or neutron diffraction. For example, the modern AFM machines, which can employ an automatic tip preparation [17], are restricted mainly by the sample preparation and are physically capable of scanning thousands of molecules per day. However, the data interpretation, typically done by teams of human experts with the aid of atomistic simulations, proves to be a tedious and challenging process. This bottleneck hampers the broader adoption of SPM-based analytical methods beyond basic research.

The probe-particle model, first introduced nearly a decade ago [5], has become a widely used tool for simulating high-resolution AFM and STM images. Unlike other AFM simulation software used in the fields of contact-AFM, soft-matter and biology [18–20] which focuses typically on mesoscopic aspects and AFM operation in the ambient condition, the probe-particle model has been developed to explain atom-resolving non-contact AFM and STM experiments carried out in ultra-high vacuum at cryogenic temperatures with decorated tips. The model enables the rationalization of experimentally observed SPM contrast and its attribution to chemical structure. The AFM part of the model, compiled to the PPAFM computation package, is the main focus of this work.

In this specific domain PPAFM provides a good accuracy of simulated images at low computational cost. This enables rapid exploration of candidate molecular or surface structures and the exploration of suitable imaging parameters to match experimentally observed contrast to an *a priori* unknown geometry. Moreover, in recent years, PPAFM has emerged as a key driver of progress in the field of automatic interpretation of AFM data using machine-learned models [21–23], as well as for the construction of large datasets [24] of simulated AFM data. To the best of our knowledge, PPAFM has served as the primary tool for generating training data for all machine-learned high-resolution AFM interpretation models published to date.

However, despite nearly a decade of development, the documentation surrounding PPAFM has been relatively scarce, leaving (potential) users largely unaware of all its features and its recent development. Therefore, in this article, we aim to present the full spectrum of capabilities offered by the latest release of PPAFM and present it as a comprehensive toolbox for high-throughput simulations, encompassing not only high-resolution microscopy AFM but also STM, KPFM, IETS, and other related SPM techniques: Section 2 describes the theoretical background of the Probe Particle Model [5] including systematic comparison of all implemented levels of theory for tip-sample interaction in order of increasing accuracy, which is missing in previous publications. There we also describe newly implemented *full-density density model* (FDBM) [25] providing substantially increased accuracy. Section 3 discusses models for the simulation of other SPM techniques such as STM, IETS and recently added KPFM, which builds on top of the AFM model. Section 4 describes the code from the user's perspective, with the emphasis on recently simplified installation through Python Package Index (PyPI) and real-time Graphical User Interface (GUI), allowing for a user-friendly introduction of new users into PPAFM usage. The technical details concerning the implementation of the method are provided in section 5, showing the acceleration gained by smart numerical implementation, and recent parallelization on both CPU and GPU allowing for speed-up by several orders of magnitude. Last but not least, PPAFM is now accompanied by enhanced documentation. We believe that these enhancements will open the field of AFM simulation towards new users and new applications in molecular design, materials science, and surface science.

2. AFM simulation models

2.1. Tip description

The original probe-particle model was based on a simple idea: simulating a non-reactive, flexible tip apex such as an attached CO molecule (or tip decoration like H_2, Xe [4], NTCDA [26] etc.) by modelling it as a single spherical particle attached to the end of an AFM tip by a lever with a bending spring. This spherical particle, which we call the *probe particle* (PP), represents the very last atom of the flexible tip apex (e.g. O atom in the CO-decorated tip). This simplistic approach is motivated by the fact that the short-range forces, that determine the measured *sub-molecular contrast* rapidly decay with distance and thus can be neglected for the other atoms of the tip-apex. This allows us to separate the forces from the tip (indexed with T) and forces from a sample (indexed with S) so that the overall force acting on the PP (F^{PP}) during its relaxation is evaluated as follows:

$$F^{PP}(\vec{r}_{PP}) = F^{T}(\vec{r}_{PP}) + F^{S}(\vec{r}_{PP}), \tag{1}$$

The forces from the sample are discussed in greater detail in section 2.2.

The model for the forces from the tip is as follows:

$$F^{T}(\vec{r}_{PP}) = -k_R(|\vec{d}| - R_0)(\vec{d}/|\vec{d}|) - \vec{k}_{x,y} \odot (\vec{d} - \vec{d}_0) \tag{2}$$

Here, $\vec{d} = \vec{r}_{PP} - \vec{r}_{TIP}$ is the displacement of the PP position $\vec{r}_{PP}$ with respect to the anchor point $\vec{r}_{TIP}$ to which the PP is attached (e.g. metallic tip apex to which the CO molecule it attached). $R_0 = |\vec{d}_0|$ stands for the equilibrium distance from the anchor point and $\vec{d}_0 = \vec{r}^{\,0}_{PP} - \vec{r}_{TIP}$ is the equilibrium displacement of PP from the anchor point (which is typically $(0, 0, R_0)$ for a symmetric tip but may be deflected in x,y to simulate an asymmetric CO tip). Finally, k_R is the radial stiffness constant and $\vec{k}_{x,y} = (k_x, k_y, 0)$ sets the bending stiffness and $\odot$ denotes

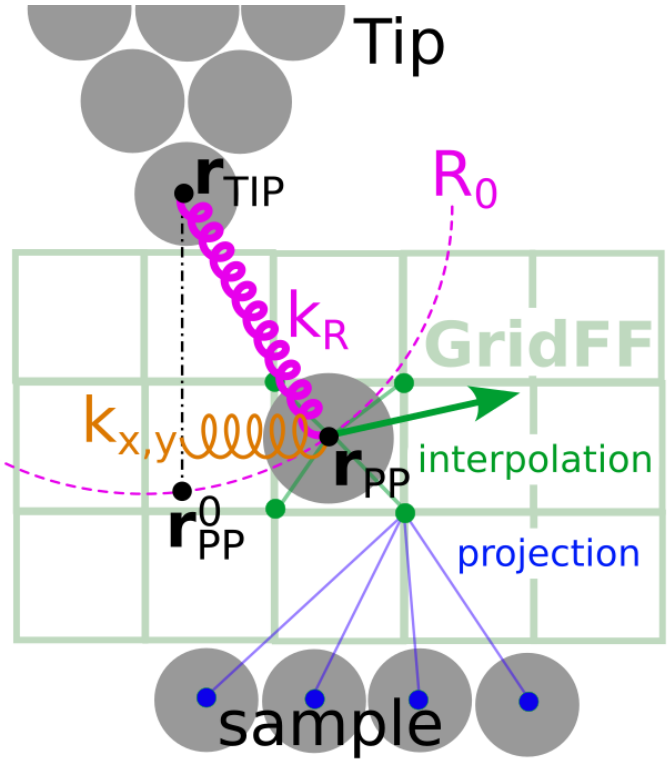

Figure 1: **Schematics of forces acting on the flexible *probe particle* (PP) in PPAFM:** The PP represents the very last atom of the non-reactive, flexible tip-apex (e.g. O atom of attached CO molecule), its position is denoted $\vec{r}_{PP}$. It is anchored to a rigid AFM tip by radial spring with high stiffness k_R which keeps it in a certain distance R_0 from the anchor point R_{TIP}, and a lateral spring $k_{x,y}$ which tries to return to equilibrium position R^0_{PP} under the tip. Besides the forces from the tip, also forces of the sample act on PP. These forces are calculated by interpolation of grid projected forcefield (GridFF). GridFF can be calculated by projection of atomic potentials (see Eq. 5, Eq. 6) or by convolution of grid projected densities (see Eq. 7, Eq. 8).

the component-wise product of vectors. This differs from the original model [5], which used the Lennard-Jones potential for the radial force, keeping the PP under the tip, while here we are using the strong spring force k_R, as this is a computationally faster and more stable solution. The lateral movement of the PP is still controlled by the lateral springs k_x and k_y as it is shown in Fig. 1(a). From our experience, CO tips are best reproduced using a lateral stiffness of 0.24-0.25 N/m [27].

The z-component of the short-range forces acting on the tip (F_z^{tip}) can then be calculated as the z-component of the radial spring force acting on the PP, $F_z^{tip}(\vec{r_{tip}}) = -F^T_{R,z}$ at the fully relaxed position of the PP, as these forces balance each other out. F_z^{tip} is then used for calculating the actually measured frequency shift Δf using the formula derived by Giessibl [28]:

$$\Delta f^{tip}(\vec{r_{tip}}) = -\frac{f_0}{2k}\frac{8}{\pi A^2}\int_{-A/2}^{A/2}\frac{zF_z^{tip}(\vec{r_{tip}}+\hat{A}z)}{\sqrt{A^2/4-z^2}}dz, \tag{3}$$

where k is the stiffness and f_0 is the base oscillation frequency of the cantilever, A is the peak-to-peak amplitude of the oscillation of the AFM tip and $\hat{A}$ is the normalized direction vector of the oscillation (typically in the z-direction).

2.2. Sample-tip interaction

The sample-tip interaction comprise of Pauli repulsion F_{Pauli}, van der Waals attraction (or London dispersion force) F_{vdW}, and electrostatic interaction F_{el} between the PP and the sample:

$$F^S(\vec{r}_{PP}) = F_{Pauli}(\vec{r}_{PP}) + F_{vdW}(\vec{r}_{PP}) + F_{el}(\vec{r}_{PP}). \tag{4}$$

The precision of the PPAFM simulation can be tuned by the level of theory describing these interactions.

In the following section, we cover the historical development of the different approximate models and their applicability. Despite the actual implementation relying on forces, for simplicity, we only discuss formulas to compute energy components. The respective formula for the force can be obtained as a derivative of the energy $\vec{F}(\vec{r}_{PP}) = -\nabla E(\vec{r}_{PP})$.

2.2.1. Lennard-Jones

In the original (and the simplest) PPAFM model [5] the motion of the PP, $\vec{r}_{PP}$, is governed by a potential obtained as a sum of pair-wise Lennard-Jones (LJ) potentials between the PP and all the atoms of the sample. The attractive and repulsive parts of LJ potential simulate the attractive London dispersion and the Pauli repulsion respectively. The total potential is evaluated as follows:

$$E_{LJ}(\vec{r}_{PP}) = e_{PP}\sum_i e_i\left[\left(\frac{R_{i,PP}}{|\vec{r}_i-\vec{r}_{PP}|}\right)^{12} - \left(\frac{R_{i,PP}}{|\vec{r}_i-\vec{r}_{PP}|}\right)^{6}\right] \tag{5}$$

Here the position of the sample atoms $\vec{r}_i$ are considered rigid (i.e. not movable), and traditional mixing rules such as $R_{i,PP} = R_i + R_{PP}$ and $e_{i,PP} = \sqrt{e_i e_{PP}}$ are used to evaluate the equilibrium distance $R_{i,PP}$ and binding energy $e_{i,PP}$ of the i-th atom of the sample and the PP. The default parameters e_i, R_i are taken from the OPLS force field [29], but PPAFM also allows for a change of the element-based parameters in a user-provided parameter file.

2.2.2. Lennard-Jones with point charge electrostatics

Already in the same year, the model was modified to include the electrostatic interactions between the tip and the sample [7].

Initially, the electrostatics was implemented as a sum of Coulomb potentials between classical point charges positioned at the centre of the PP (q_{PP}) and the sample atoms (q_i):

$$E_{el}(\vec{r}_{PP}) = k_e q_{PP}\sum_i \frac{q_i}{|\vec{r}_i-\vec{r}_{PP}|}, \tag{6}$$

where k_e is the Coulomb constant. Simultaneously with improvements of the physics captured by the PPAFM model, the assumption of a rigid sample allowed significant optimizations and acceleration of the simulations. Both the electrostatic and the LJ force field are pre-calculated and stored on a real space grid, from which they are interpolated during the simulations, as illustrated in Fig. 1 and explained in sec. 5.1.

2.2.3. Lennard-Jones with density functional theory based electrostatics

A more accurate model of the electrostatics was developed in the same year using a grid-based real-space representation of electrostatic potential of the sample (V_S). V_S is obtained as the Hartree potential from sample electronic structure calculation from density functional theory (DFT). The electrostatic potential acting on the PP with its charge density (ρ_{PP}) is obtained through a cross-correlation integral:

$$E_{el}(\vec{r}_{PP}) = \int_{\vec{r}} \rho_{PP}(\vec{r} + \vec{r}_{PP}) V_S(\vec{r}) d\vec{r}. \quad (7)$$

We found that the distortions in AFM images by electrostatic field to a large extent explain for example the over-enhanced bond-length contrast in fullerenes or other Kekule structures [8, 30] but also the repulsive contrast over triple bonds and free electron pairs [9]. Nevertheless, the charge required to reproduce experimental contrast with monopole charge distribution was unrealistically high (0.2-0.4e).

In further applications [31–33] we concluded that the quadrupolar charge distribution better reproduces contrast observed with CO-tip. The quadrupolar charge distribution is better fitting the CO molecule and CO-tip charge density as concluded by DFT calculations [25, 32].

While point-charge electrostatics proved useful for quick and easy model calculations independent of ab initio inputs, which were often conducted by external experimental groups through a web interface [34], DFT-based electrostatics of the sample was, nevertheless, found necessary to properly simulate intricate image effects, such as those arising from free electron pairs and triple bonds. For the CO tip the quadrupole moment can vary in between -0.025 to -0.15 $e \times \text{Å}^2$, depending on the experiment [21, 31, 35].

A minor disadvantage of the cross-correlation-based approach (see sec. 5.1) is the assumption that the PP moves without rotation However, according to our experience with the complex-tip model [36] and comparison of our PPAFM model against the direct integration model by Ellner at al. [25] the differences caused by the multipole rotation are minor. This can be understood from the fact that bending angles are rather small at tip-sample distance relevant for high-resolution imaging experiments, and the bending is most significant at the close range where the interaction is dominated by the Pauli rather than electrostatic interaction.

2.2.4. Full density-based model

Pauli repulsion modeled by the repulsive part ($1/r^{12}$) of the spherically symmetric LJ potential cannot reproduce delicate effects emerging from rearrangements of the electron density in the sample which are often visible using HR-AFM techniques [8–10]. Some of these limitations can be mitigated by modification of the LJ parameters of individual atoms (especially van der Waals radius) to match the iso-surface of electron density obtained from a DFT calculation [10]. This approach allows to distinguish between different occupations of the atomic orbitals for atoms of the same element and it was also successfully used for calculations of ionic materials, such as calcite or calcium fluoride [15, 16]. Nevertheless, such approach is still limited by the spherical symmetry of the LJ potential, therefore it cannot fully recover non-spherical effects such as free-electron pairs and variation of density in covalent bonds.

In order to addresses these limitations, Ellner et al. [37] introduced an improved model called the *full density-based model* (FDBM), where both the Pauli repulsion and electrostatics are calculated directly from electron density obtained from DFT. While electrostatics is still calculated using Eq. 7, the Pauli repulsion is newly calculated by the integral of the product of the tip and the sample charge densities scaled by a fitting constant A. Eventually the product is raised to exponent β (although β is typically close to one):

$$E_{Pauli}(\vec{r}_{PP}) = A \int_{\vec{r}} [\rho_{PP}(\vec{r} + \vec{r}_{PP}) \rho_S(\vec{r}))]^{\beta} \, d\vec{r} \quad (8)$$

The magnitude of the repulsion is significantly more sensitive to the exponent β than the multiplicative factor A. Even a change of only 0.1 in β results in a significant change in the observed contrast, higher values typically resulting in reduced sharpness. However, if the scanning distance and A are adjusted along with β, similar-looking contrast can be observed with multiple distinct combinations of the parameters.

The resulting model, combined with an appropriate dispersion interaction model (previously modeled by the attractive part of the LJ potential), and properly fitted, could remarkably reproduce experimentally measured images of rigid molecules. Particularly, it better captures the free electron pairs (e.g., oxygen and nitrogen heteroatoms) and Kekule structures (e.g., triple bonds), which were previously only emulated through the repulsive electrostatic field in the original LJ -based model sometimes using unrealistically high tip charge [30]. Now FDBM also accounts for Pauli repulsion, capturing the electron hardness of free electron pairs on oxygen and nitrogen atoms.

The dispersion interaction model typically used with the FDBM is the Grimme DFT-D3 [38] dispersion correction, which we have also recently implemented in PPAFM, in particular in the Becke-Johnson damping form [39]. One notable aspect of the DFT-D3 correction is that the interaction coefficients for each atom depend on their chemical environment, based on proximity, in order to account for the changing polarizability due to bonding. In principle the distance calculations to determine the bonding configuration would also include the PP. However, since the PP is supposed to be chemically inert, we choose to exclude the PP from this calculation, which allows the interaction coefficients in the sample to be calculated independent of the PP position, significantly speeding up the calculation.

The DFT-D3 energy also has parameters that are adjusted for particular DFT functionals - namely s_6, s_8, a_1, and a_2 [38]. So far there has not been any extensive study on the effect of these parameters on PPAFM simulations and thus we recommend to stick to the parameters connect with the DFT functional used for calculation of the FDBM models input. PPAFM provides here predefined parameter values for many of commonly used DFT functionals.

2.2.5. Comparison of AFM simulation models

In order to illustrate strengths and weaknesses of each tip-sample interaction model we plot in Fig. 2 results calculated for a representative selection of molecules. We compare our PPAFM simulations against a DFT reference calculations performed via CP2K [41] with PBE exchange-correlation functional and Grimme DFT-D3 [38] used for the van der Waals correction. Each of the selected molecules represent some characteristic chemical moieties manifested as characteristic features in AFM and was previously discussed in HR-AFM related literature. To make the comparison consistent we choose same simulation parameters for each molecule, even though this choice may not be optimal to represent the DFT reference or experimentally observed contrast. This means that for FDBM model we set the multiplicative factor $A = 12$ and exponent $\beta = 1.2$ (see Eq. 8), which provided best overall match to DFT for all the molecules. We found that the best match is visible if we offset z-distance by -0.2 Å between the DFT and the PPAFM simulations in order to get a roughly matching level of sharpness in the observed contrast. In the FDBM simulation the electrostatics used a DFT-calculated charge density on the CO-tip. For the Lennard-Jones based simulation model (both with point-charge and Hartree potential) the we used quadrupole charge distributions on the tip with quadrupole moment $-0.05\, e \times$ Å^2. For point charges simulations we used Mulliken charges reported by FHI-aims [40].

C60 Fullerene was studied as an example of bond order discrimination [8]. Difference in the apparent bond length, as well as the ovaloid shape of electron cloud is very well reproduced by the FDBM model. To some degree the difference in apparent bond length can be reproduced also with the LJ+Hartree model, nevertheless unrealistically high charge of the tip is needed to reproduce experimental (or DFT calculated) contrast [30].

FAD (Formic acid dimer)) represents carboxylic groups which often dimerize in self-assembled structures studied by AFM [9, 42]. The FDBM again provides contrast most similar to DFT data, including bright spots above oxygen atoms. This is due to ability of FDBM to reflect localized electron pairs in Pauli repulsion. Nevertheless these bright spots are visible also in LJ+PC and LJ+Hartree simulations at higher tip-sample separation where electrostatic forces dominate [9].

FFPB molecule (4-(4-(2,3,4,5,6- pentafluorophenylethynyl)-2,3,5,6- tetrafluorophenylethynyl) phenylethynylbenzene) was studied to see the effect of electron depletion on the AFM contrast in a benzene ring (π-hole), caused by the electron withdrawing substituents (fluorines) [43, 44]. In DFT simulations this is visible as darker contrast over fluorinated rings, which can be attributed to a faster decay of the electron density [45] (due to deeper electrostatic potential and lower work function) and by electrostatic attraction between the (π-hole) and free electron pair of CO tip. Surprisingly, this effect is best reproduced by LJ+PC model, which used Mulliken charges obtained from DFT calculation. Another characteristic feature is the triple bond rendered as bright line perpendicular to the bond. This effect is caused by the toroidal shape of the π-electron cloud around the triple bond [9, 46], which produce a quadrupolar field both in electrostatics and Pauli repulsion. FDBM again reproduce this feature best thanks to incorporation of proper aspherical Pauli repulsion, while the Lennard-Jones potential is composed of spherical potentials around each atom and therefore cannot reproduce this feature. Nevertheless both LJ+PC and LJ+Hartree can reproduce the electrostatic contribution of this repulsive feature.

Pentacene molecule was one of the first molecules for which bond-resolved AFM images were measured [3]. Beside the five hexagonal rings the experiment and DFT simulations shows clearly increased repulsion over the ends of the aromatic system. This effect is to a large degree caused by higher attractive van der Waals background in the center as was explained in original paper [3]. Nevertheless our simulation done at closer tip-sample separation shows, that the effect is pronounced even at distance where van der Waals contribution is negligible. This is reproduced by FDBM but not with LJ-based models. Without detailed analysis we can only speculate that this is because tails of occupied frontier molecular orbitals (HOMO, HOMO-1 etc.) which contribute most to Pauli repulsion are more supressed in the center due to presence of nodes. All models including FDBM and LJ-based models reproduce very well the distortion (elongation) of the rings perpendicular to the molecule axis, which is caused by deflection of the probe mostly due to lateral gradient of van der Waals potential (with a slight contribution from electrostatics), as was discussed previously [31, 47].

Phtalocyanine molecule was widely studied in the SPM community [10, 48–50] due its great potential for molecular electronics and catalysis, and for biological importance of porphirine derivatives. The main features which can be seen in HR-AFM experiments and which are perfectly reproduced by DFT simulations are: (i) The bright peripheral benzene rings contrasting against the darker porphirine center, and (ii) sharp pointy corners of imine nitrogens. Both of these features are nicely reproduced by FDBM, which properly accounts for the Pauli repulsion affected by slower decay of electron clouds in benzene rings (with respect to the porphirine center), as well as Pauli repulsion of the free electron pairs of these nitrogens. The LJ-based model incorrectly renders the pentagonal rings brighter. This is a simple effect of higher concentration of repulsive atoms in the pentagon ring in contrast to the hexagon , as the LJ model cannot account for rate of decay of tails of electron density. Nevertheless, the pointyness of the nitrogen groups is rather well reproduced mostly due to the significant role of the electrostatic forces which cause apparent shrinking of these areas as previously discussed [7].

PTCDA (Perylenetetracarboxylic anhydride) is perhaps the most studied molecule in the SPM community [4, 5, 31, 45, 51], mostly due to experimental convenience and formation of well ordered self-assembled monolayers. The experiments as well as DFT simulations show the central perylene system considerably brighter than the peripheral anhydride groups. This is more-or-less reproduced by all models, although FDBM model excels in this aspect, as it reflects higher Pauli repulsion due to the longer extent of the electron cloud over the perylene system [45]. All models properly describe apparent enlargement of the anhydride groups and shrinking of the perylene group

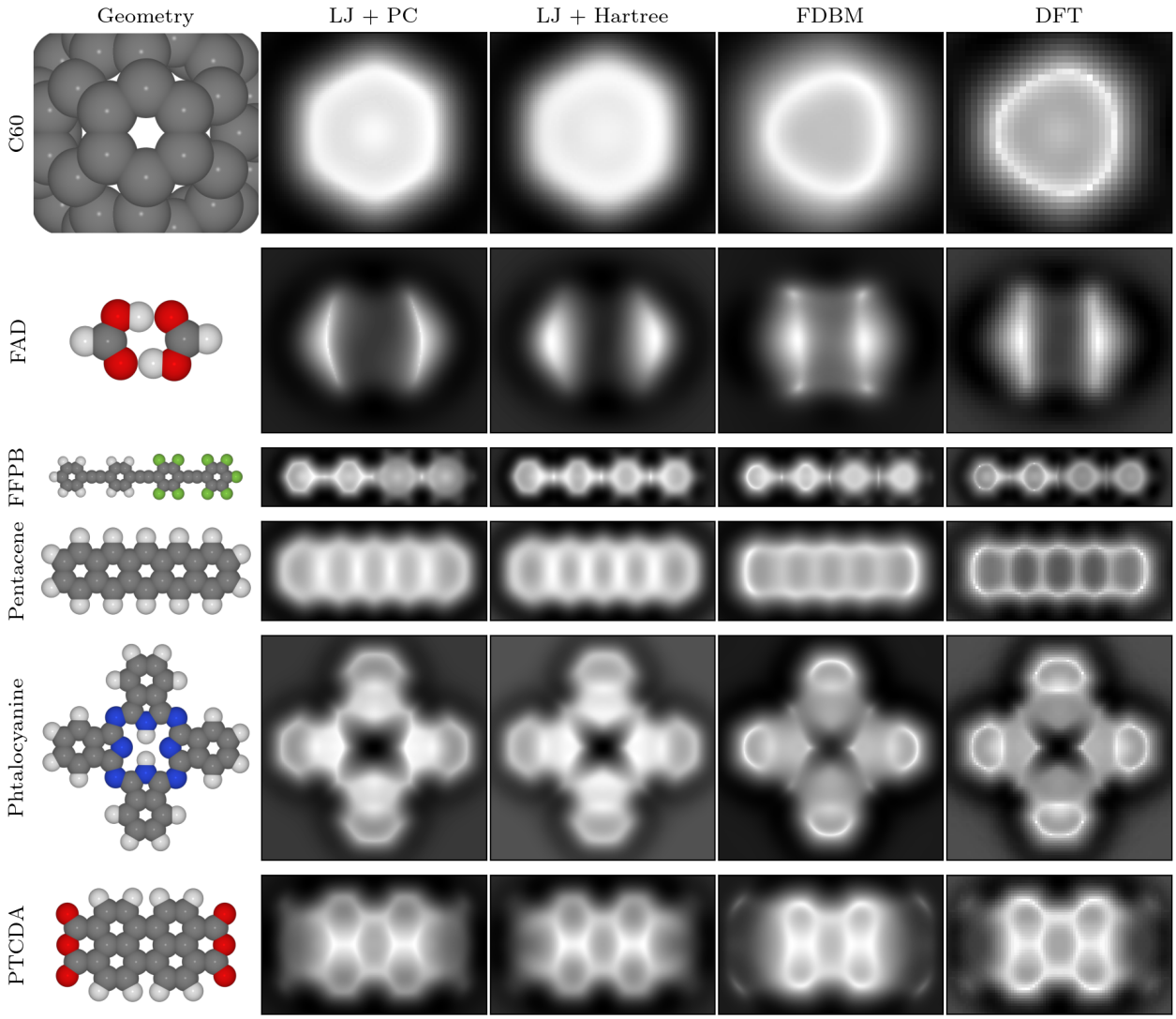

Figure 2: **Comparison of PPAFM simulations with different models of tip-sample interaction.** The columns depict different models. Starting from the left, they are Lennard-Jones + point charges (LJ+PC), Lennard-Jones + Hartree (LJ+Hartree), Full density based model (FDBM), and a DFT simulation used as a reference, where tip-sample interaction at each pixel was calculated as an independent relaxation of the tip using the CP2K program. For the Lennard-Jones based simulation model (both with point-charge and Hartree potential) we used a quadrupole charge distributions on the tip with the quadrupole moment $-0.05\,e \times \text{Å}^2$. For the point-charge simulations we used Mulliken charges reported by FHI-aims [40]. For FDBM model we set the multiplicative factor $A = 12$ and exponent $\beta = 1.2$ (see Eq. 8) which provided best overall match to DFT for all the molecules.

caused by electrostatic forces [31]. In addition, the DFT simulation shows bright repulsive features over the carbonyl oxygens, which are again best reproduced by FDBM model.

Despite generally superior accuracy of the FDBM approach, the PPAFM code allow users to choose from various simulation models (Lennard-Jones, Morse, point charges, model charge density integration, FDBM) the one which offers an optimal compromise between accuracy and simplicity for their particular application. Such a choice should not be motivated by computational cost of AFM simulations, as our efficient GPU implementation allows interactive simulations even on the FDBM level.

Nevertheless, the simpler models (e.g., LJ + point charges) limit reliance on DFT data (i.e. charge density and Hartree potential are not required). This makes those simple models very convenient for fast screening over various modeled sample geometries or creation of databases for machine learning approaches. The dependence of the DFT electrostatics and FDBM method on DFT calculations (at least thousand times slower) and large amount of volumetric data are making this method less attractive for fast high-throughput simulation scenarios. For rapid training of AFM recognition models, we recommend pre-training the model on the data obtained from simple LJ and point-charge-based simulations, with the refinement step performed on fewer examples generated by the FDBM (similar approach was used in [23]).

Notice that LJ simulations presented in 2 were done using default LJ parameters which depend only on chemical elements, not on more detailed atomic types (i.e. we do not distinguish different sub-types of carbon like sp^1, sp^2, aromatic, carboxylic

etc.). With more careful selection of atomic types and of LJ parameters (particularly the atomic radius) even the simple LJ model can simulate the different extent of electron clouds and bring LJ-PC model closer to AFM experiments without the need of DFT inputs [10, 16]. Although FDBM model does not depend on such detailed choice of atomic types (assuming van der Waals D3 parameters are given, and has minor effect on resulting contrast), it still depends on the choice of the two global parameters (scaling factors A and exponent β in Eq. 8). Optimal choice of these two parameters is still under debate, and may be system dependent.

3. Other PP-SPM simulation modes

AFM simulation models discussed in previous section are the central part of probe-particle simulations as they determine forces acting on the PP and therefore also its relaxation (deflection). This deflection then modifies the measured contrast of other signals (such as STM [5, 6] and IETS [7]), typically by sharpening or introducing discontinuities to the contrast. In addition, other forces can emerge in the junction between tip and sample e.g. due to polarization of the PP or the molecule under study by external electric field. These microscopic contributions of the polarization force which is responsible for the *submolecular* contrast in Kelvin probe force microscopy (KPFM) can be also simulated within the PPAFM framework. The following section discusses simulation techniques of all these different techniques which are built on top of the PPAFM core.

3.1. Kelvin probe force microscopy

Traditionally, KPFM experiments measured the electrostatic forces between tip and sample due to external electric potentials and differences between the work functions of the two materials. In this process the tip and the sample can be seen as the plates of a capacitor. The force between such plates depends quadratically on the potential difference between the tip and the sample V and linearly on the gradient of the effective capacitance $C(\vec{r}_{tip})$ with respect to the position of the tip.

$$\vec{F}(\vec{r}_{tip}) = \frac{V^2}{2}\nabla C(\vec{r}_{tip}). \tag{9}$$

Although KPFM experiments were originally intended to measure mesoscopic features such as the work function of the studied materials and long-range charge domains, the development of atomically precise SPM techniques had allowed to achieve *sub-molecular* KPFM contrast, corresponding to variations of the charge distribution and polarizability within individual organic molecules [43, 49, 52, 53]. Nevertheless, the quantitative relation between the measured quantities and the electronic structure of the molecules was under debate. We developed a Kelvin Probe Force Microscopy modality into the PPAFM code in order to put these relations on quantitative ground and provide a straightforward tool for the simulation of these phenomena.

In this implementation, the bias dependence of both the charge density of the probe and the electrostatic potential of the sample is introduced in Eq. 7, to study its effect on the force $\vec{F}_{PP}(\vec{r}_{tip})$ and the corresponding frequency shift Δf. As has been shown in our previous publications [44, 54], the *submolecular* variation of $\Delta f(V)$ originates mostly from the intrinsic charges within the tip or the sample that interact with bias-induced electric polarization of the opposite electrode. The output of the KPFM mode can be represented as a map of (apparent) *local contact potential difference* (LCPD or V_{LCPD}), which corresponds to the bias voltage at which the maximum of the (approximately) parabolic $\Delta f(V)$ dependence lies.

Currently, the KPFM functionality is implemented in the PPAFM package in two variants. In the first version, the changes in the charge densities of the tip and sample due to the application of an external field in the z-direction must be provided as inputs from external DFT calculations. In the second version, analytically generated tip polarizations, fitted to the DFT calculated ones, are provided for user convenience. For a more detailed description of the usage of the KPFM module and the theoretical basis of the model, please refer to the code manual and the supplementary information of [54].

As an example of a KPFM simulation, Fig. 3a shows the LCPD map over the FFPB molecule. The LCPD is affected by the local electric charges on the molecule: positive charge under the tip tends to shift the LCPD towards more negative values, negative charge towards more positive values. The resulting figure clearly shows the polarization within the molecule. The

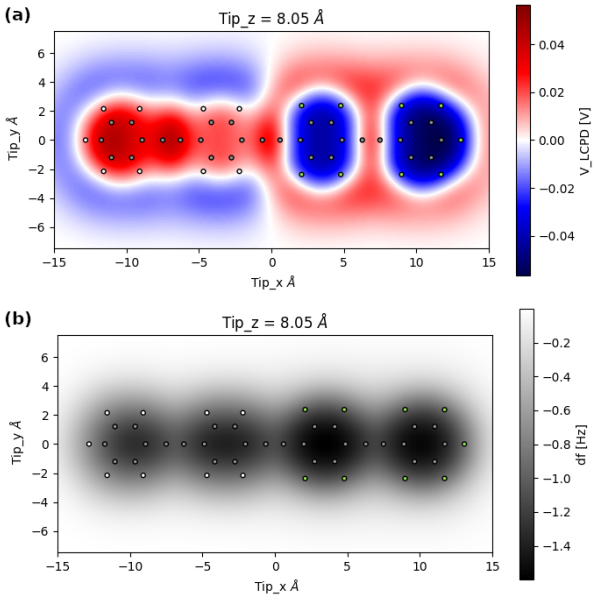

Figure 3: (a) LCPD map taken over the FFPB molecule, simulated using the KPFM functionality of PPAFM. (b) AFM image for the same tip distance as in the LCPD map. Images in both panels are overlaid with atomic structure of the FFPB molecule. The Tip_z = 8.05 Å distance quoted as the height of the scanning plane position was measured between the molecular plane and the anchor pivot (metallic apex) of the tip. The tip distance z_{tip} = 4.05 Å used to scale the electric field induced by the voltage between the tip and the molecule was smaller by R_0 = 4.00 Å. A CO-tip model with the static quadrupole moment of $-0.05\ e \times$ Å^2 and default electric polarizability was used. The capacitance of the metallic part of the tip was modeled with a sphere of the R_{tip} = 40 nm radius.

two positive-charged (electron-depleted) benzene rings in the right-hand-side half of the molecule are surrounded by negative charge of the fluorine atoms, while the two electron-rich benzene rings in the left-hand-side half are surrounded by more positive hydrogen atoms. Notice that the simulated contrast is consistend with experimentally measured KPFM pictures from literature [43]. KPFM experiments usually need to be performed with larger tip–sample distance as compared to HR-AFM , resulting in much blurred AFM image (Fig. 3b) in comparison with the HR-AFM of FFPB in Fig. 2.

3.2. Bond-resolved STM

Despite the fact that the bond-resolved STM technique preceded *sub-molecular resolution* in the AFM [4], this technique received less attention in scientific community because the interpretation of the measured signal was unclear. In order to put the interpretation of these techniques on more quantitative grounds, and provide a straightforward simulation tool, we developed PPSTM [6, 55] which builds on top of PPAFM. The PPSTM code can be used as a standalone STM simulation package (independent of PPAFM) to simulate normal STM with rigid (e.g. metallic) tip. It is based on Chen's rules [56] approximation of Bardeen tunneling theory to evaluate tunneling current between the tip and sample.

Nevertheless, the real strength of the PPSTM code is in its capability to calculate high-resolution (i.e. bond-resolved) STM images obtained with flexible tip-apices (e.g. CO, Xe, H_2) on organic molecules. In this application PPSTM is combined with the PPAFM code for pre-calculating the PP positions $\vec{r}_{PP}$ for each position of the tip $\vec{r}_{tip}$ during the scanning. This essentially just shifts the position of the orbitals located on the PP involved in the Chen's tunneling formulas, as is illustrated in Fig. 4(a), which distorts the resulting image and gives rise to the characteristic sharp contrast in the high-resolution STM images as was described in [5, 6]. Bond-resolved imaging and STM simulations can be especially beneficial for STM machines without AFM possibilities, since STM measurements are tipically experimentally simpler than AFM. This was used for example for study of carbon nanoribbons and other graphitic structures [57, 58].

The main drawback of this approach is the added complexity of the interpretation and theoretical rationalization of the measured STM signal, which depends both on geometrical relaxation of the PP as well as on precise estimation of elusive electronic structure of the sample, and the tip [6], as is illustrated in Fig. 4(b) and (c). Precise hybrid functional DFT calculations of the whole sample (i.e. including both molecule and substrate) are often necessary in order to achieve agreement with experiment [35].

3.3. Inelastic scanning tunneling microscopy

Another method to achieve *sub-molecular resolution*, very close to the HR-AFM contrast, was demonstrated by the Ho group with inelastic STM [59]; however, without explanation of its mechanism. Already in the same year we were able to explain and simulate the observed contrast with the new IETS

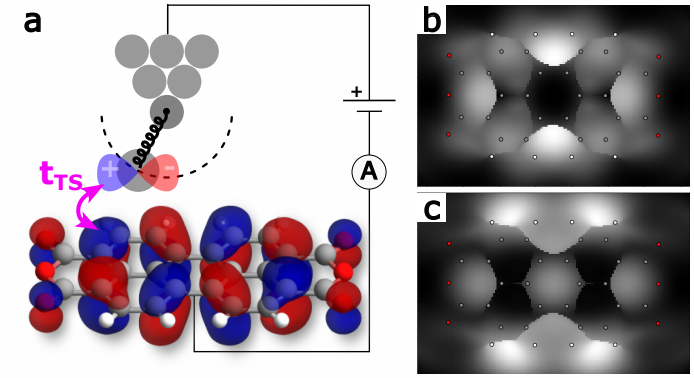

Figure 4: **Schematics of PPSTM with example of PTCDA**. (a) PPSTM calculates the electron tunneling rate T_{TS} between the molecular orbitals of the sample and the tip using Chen's rules [56]. The orbitals of the tip are modeled by atomic orbitals, like s, p_z, p_x (on the image) and p_y, positioned at the probe particle. This is done for the PP positions previously relaxed by PPAFM in order to account for the displacement of e.g. a CO molecule caused by the interaction with the sample. (b,c) Examples of a simulated PPSTM of the PTCDA molecule image using the *dIdV* mode. The model electronic structure of the tip was chosen to be 13% of s PP orbital and 87% of p_x and p_y orbitals. This configuration best reproduced experimentally observed contrast measured with CO-tip in the previous publications (e.g. [35]). (b) at the sample bias corresponding to the HOMO orbital energy. (c) at the sample bias corresponding to the LUMO orbital energy. Please note that in the experiment the STM contrast can be affected by interaction of molecular orbitals with the interface states the substrate, forming a delicate electronic structure.

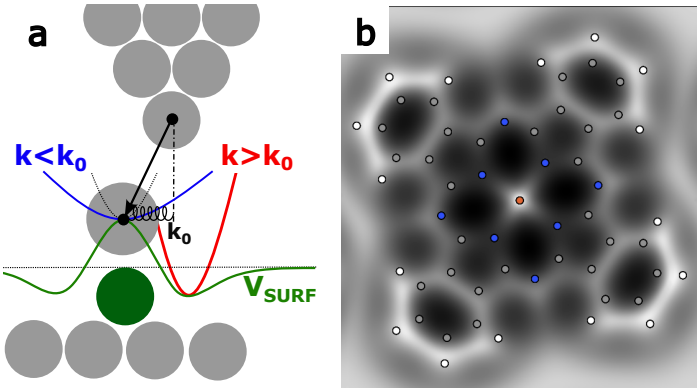

Figure 5: **PP-IETS with example of Iron Phtalocyanine (FePc)**. **(a)** Schematic illustration of the PP-IETS imaging mechanism. The stiffness of the lateral CO vibration (k_0) is modified by curvature of the tip-sample interaction potential V_{surf}. The stiffness as well as the associated vibration frequency is increased at the position of a convex V_{surf} and decreased at position of a concave potential (e.g. above atoms and bonds). Due to broadening of peaks measured in IETS spectroscopy, this softening of the modes above atoms and bonds allows detecting higher amplitude of inelastic tunneling signal originating from lateral CO vibration below the base energy ϵ_0 associated with the base stiffness k_0, as was done by the Ho group [59]. For a more detailed explanation please see [7, 35]. **(b)** Example of an IETS map calculated by PPAFM on the iron phtalocyanine (FePc) molecule using just a Lennard-Jones force-field. Notice that in this particular simulation neither the distortions caused by electrostatics as discussed in [7] nor the modulation of the tunneling signal by orbital symmetry discussed in [35] are present.

module added to our PPAFM package [7]. This module calculates the change of the stiffness (resp. vibration frequency) of lateral vibration modes of the CO molecule attached to AFM tip due to its interaction with the sample (see Fig. 5a). In repulsive

regime the ridge-lines in tip-sample interaction potential (e.g. over the bonds between atoms in the sample) introduce negative curvature to the total potential in which the CO molecule vibrates. This effectively decreases the stiffness and vibration frequency of the relevant vibration mode, therefore shifting the inelastic tunneling peaks to lower energy. This effect is visible in simulated map shown in Fig. 5b, where bright contrast above the atoms and bonds correspond to increased inelastic tunnelling signal at energy (i.e. bias voltage set-point) below the base energy of lateral CO vibration mode. The amplitude of the peak is related to shift of the peak energy when considering e.g. Gaussian broadening as explained in [7].

Later we were able to improve this technique through considering the variation of the tunneling current, which depends on the orbital symmetry [35]. The inelastic signal modulation via the electron-phonon coupling between the tunneling (calculated by Chen's rules as in section 3.2) and the lateral vibration mode, are described in detail in [35].

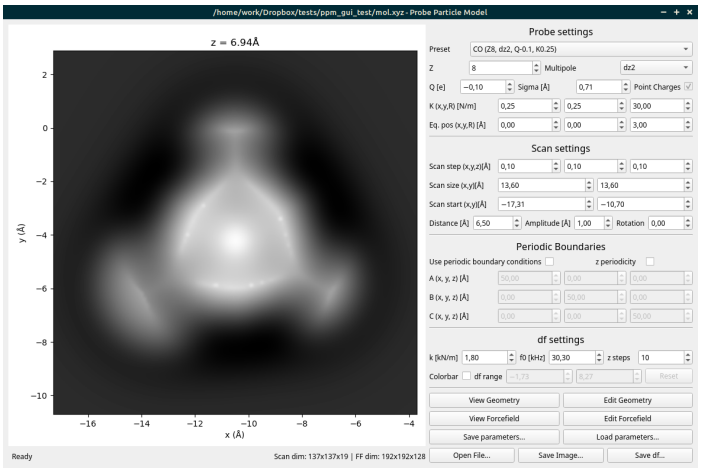

Figure 6: Interactive GUI for GPU-accelerated PPAFM simulations. The user can interactively modify imaging parameters by using input boxes or a mouse-wheel, and image contrast is updated automatically.

4. PPAFM from the user perspective

4.1. Installation

The default way to install the PPAFM code is through the pip installer for Python packages. This can be achieved by running

```
pip install ppafm
```

on the command line. This installs the package from the Python Package Index (PyPI), which contains pre-compiled distributions of the PPAFM code for several operating systems. If the binary files for your environment do not exist, the "pip" tool will attempt to compile them upon download. Additionally, pip installs all the necessary Python dependencies. Some non-Python GPU dependencies, however, might be installed separately from appropriate OpenCL-capable GPU drivers and related libraries. For more experienced users and developers we provide alternative ways of installing and running the code. The most up-to-date installation instructions can always be found in the repository [60]. They include installation in a dedicated Conda environment, Docker container, building from the source code, and others.

4.2. Command-line user interface

The command-line interface (CLI) of the PPAFM code provides users with access to the full capabilities of the package. This is an alternative to the graphical user interface discussed in the following section. The CLI interface allows to run simulations on supercomputers, cloud computers, and other computational resources without a graphical interface. Also, the CLI interface is used for high-throughput simulations when run by a workflow manager.

Once the PPAFM package is installed user gets access to a variety of tools to compute force fields, relax the probe particle, and plot the results. Below is an example of launching PPAFM to compute the Lennard-Jones force field:

```
ppafm-generate-ljff -i structure.xyz
```

In the example above we specify an XYZ file with an input structure. Additionally, the user can create a "params.ini" file containing more fine-tuning settings of the simulation. If the file is present in the folder, the code will pick it up automatically. The PPAFM repository [60] contains detailed instructions on how to use PPAFM throught the CLI.

4.3. Graphical user interface

The latest GPU-accelerated version of the PPAFM code is so fast that interacting with the user solely through scripts or a bash terminal becomes a significant bottleneck. Simulations of a full stack of AFM images with typical resolutions of 200x200x20 pixels take ~0.1 s on a typical desktop computer equipped with a dedicated GPU. For this reason, we have developed a simple graphical user interface (GUI) (see Fig. 6) that enables users to quickly explore simulation results obtained with different inputs. Users can vary parameters such as the bending stiffness of the CO tip, oscillation amplitude of the AFM cantilever, effective charge of the tip, or parameters of the FDBM model, and immediately visualize the results for comparison with experimental references. This approach is particularly useful for new users who are trying to familiarize themselves with the code and gain intuition about how various imaging parameters can affect measured AFM contrast. This exploration can be also useful to the experimentalist who wishes to gain an idea of what to expect from the images from a real HR-AFM machine. Another application is manually finding the set of parameters that most closely resembles a specific set of reference AFM images obtained with a particular setup. This can be used, for example, in the refinement of training data for machine-learned models of automatic image interpretation.

4.4. Integration with other software

In order to fully exploit the computational efficiency of the PPAFM code (especially in GPU-accelerated version) for machine-learning and other high-throughput applications, we provide a Python application programming interface (API)

which allows for seamless integration with other Python-based software. In particular, this API was used to rapidly generate training data for a machine-learning application for automated AFM image interpretation [21].

The Python API is structured in multiple levels that reflect the different computational steps in the PPAFM simulation. On the high level, the user can simply provide a molecular geometry or Hartree potential from a DFT calculation, construct a simulator with given physical parameters, and run the whole simulation in one step. On the lower level, the user could choose to manually construct the PP-sample force field with the different chosen force field models (sec. 2.2) or run the PP relaxation for a given force field.

The API also provides tools for easily creating large datasets of AFM simulations for machine learning applications. In particular, this was used in a previous study by Alldritt et al. [21], who used so-called image descriptors for identifying the atomic structures of molecules. PPAFM provides implementations for several different image descriptors that the user can compute for a given molecular geometry. In order to create datasets of both AFM simulations and any desired image descriptors, we provide a high-level generator API that takes a list of samples (geometry, Hartree potential) as an input and generates batches of samples containing the AFM images, the descriptors, and the molecule structures, ready for use in machine-learning training as is or for storing on the disk for later use. Additionally, it is possible to introduce randomizations to the simulation parameters during the generation process to account for parameters varying during the experiment, either from a predefined list of randomization operations or custom user-defined operations.

5. Implementation Details

5.1. Numerical methods

5.1.1. Grid force-field

In order to accelerate the relaxation the PP interacting with the sample we split the simulation into two steps:

1. **Force field generation**: The first step involves projection of all components of the sample potential and force-field (i.e. electrostatic, Pauli, van der Waals, see Eq. 4) onto a uniform rectangular real-space grid covering the whole simulation supercell. This means, that for each such grid point we sum atomic contribution in Eqs. 5 and 6 from all atoms of the sample, or evaluate the integrals in Eqs. 7 and 8.

   A typical spacing of the grid points is 0.1-0.2 Å which produces 1-10 million sampling points for typical simulation supercell of size 20x20x20 Å. In the CPU implementation the components of these grid force-fields are typically saved into files (e.g. FFLJ_[x|y|z].xsf, FFel_[x|y|z].xsf). In the GPU implementation this is typically not done, since saving and loading of these data files from disk is often slower than the evaluation on GPU.

2. **Relaxation**: In the second step, the PP position is optimized by the FIRE relaxation algorithm [61] using the forces interpolated from previously constructed grid force field. Currently we used tri-linear interpolation of the forces (which corresponds to quadratic interpolation of the potential). But we are experimenting with tri-cubic interpolation of the potential which may allow us to use larger grid spacing and avoid storage of forces (i.e. improve memory efficiency).

In practice, the two-step simulation procedure was found to be approximately 10-100 times faster than implementation not using an intermediate grid-based force field for typical samples comprising of tens to hundreds of atoms. The simulation speed of the two-step procedure is typically limited by the first step (force field generation), which takes roughly 1 minute on a single CPU for typical grid size comprising of a million points (100x100x100). In the case of Lennard-Jones and point-charge electrostatics the algorithm is perfectly parallelizable and it scales proportionally to number of CPUs when OpenMP acceleration is used (which is on by default in the CPU version) and it takes just ~0.1 s when using OpenCL accelerated code on contemporary GPU equipped desktops with thousands of cores.

5.1.2. Convolution theorem

The evaluation of the electrostatic force-field from the electrostatic potential of the sample and the tip charged density distribution Eq. 7 and the evaluation of the Pauli repulsion from the overlap of the sample and tip charged densities Eq. 8 have the form of a cross-correlation. Therefore they can be expressed using the convolution theorem simply as a product in the Fourier space (with an additional complex conjugation in the cross-correlation case). For a typical grid size (e.g. 100x100x100 = 1 million points) such transformation using Fast Fourier transform is orders magnitude faster than direct integration of the formulas Eq. 7, Eq. 8 point-by-point in real space (the scaling is $O((n\log(n))^3)$ for FFT vs $O(n^6)$ for direct integration, where $n = 100$ is the grid dimension in one direction). The calculation of Eq. 7 and Eq. 8 using FFT was implemented on both CPU and GPU and the computational cost is similar to Lennard-Jones and point-charge electrostatics. In the current implementation the CPU version computes the FFT using NumPy [62] (not parallized) and the GPU version uses Reikna [63].

5.2. Code structure

5.2.1. Python package with a C++/OpenCL backend

PPAFM code is designed to behave as standard Python package and exposes a Python front-end to the user, allowing sophisticated scripting. Python (with NumPy) is used to implement of the high-level logic, and most of utility functions for saving and loading simulation parameters, molecular geometry and some operations on 3D datagrids. Matplotlib library is used for plotting of final results. The computational core of the package is implemented in C++ (for CPU version) and OpenCL (for GPU version). The C++ code is interfaced with Python using the ctypes-library in Python.

5.2.2. *GPU implementation*

Modern graphics processing units (GPUs) possess thousands of independent computing cores, offering orders of magnitude higher raw computing power than traditional CPUs. However, efficient utilization of this computing power is limited to tasks that are naturally parallel (i.e., independent) and not memory-bound (either by main memory bandwidth or cache size). AFM simulations are ideal for GPU acceleration since the simulations of individual pixels (i.e., positions of the AFM tip) are virtually independent. Furthermore, the simulation scheme that evaluates the sample potential through interpolation of the real-space grid can be accelerated using texture interpolation hardware. Therefore we ported all performance intensive tasks on GPU using pyOpenCL. This includes the FFT convolution, projection of atom-wise Lennard-Jones, electrostatic, and D3 van der Waals force fields to the grid, and relaxation of the probe particle position). Generally speaking, the GPU accelerated simulations are so fast that the timing is relevant only for interactive work (GUI) or high-throughput tasks such as machine learning.

5.3. *Performance*

We conducted thorough performance tests (see Fig. 7) on periodic (infinite) graphene sheet using different levels of theory (see section 2.2) and hardware (both CPU and GPU). The simplicity of this test system allows us to systematically scale the simulation size in broad range by varying the size of the simulation box, when both the number of atoms n and grid points m scales proportionally at the same time. Therefore we can plot both on the same x-axis. Figure 7a shows the comparison of total simulation time of different methods (Lennard-Jones + point charges (LJ+PC), Lennard-Jones + Hartree (LJ+Hartree), and full-density-based model (FDBM)) on a desktop GPU. Notice the comparable performance cost and rather ideal scaling for all methods over the whole range of system sizes. The exceptions are the smallest systems (<10 atoms), where initialization and other overheads become the bottleneck. For small systems the LJ+PC method is ~2x faster than FDBM, while for system with >200 atoms FDBM actually becomes cheaper.

This can be rationalized by different asymptotic scaling of the algorithms. While the projection of the atomic force field on the grid used for calculating the Lennard-Jones and point-charge electrostatics scales as $O(nm)$, the FFT-based cross-correlation used to compute the Hartree and Pauli potentials in FDBM scales as $O(mlog(m))$ with the grid size m and is notably independent of the number of atoms n. The LJ+Hartree method using combination of both algorithms is in between LJ+PC and FDBM method. It should be noted that execution time relationship could vary for different types of systems, e.g. a non-periodic system with empty space on the sides of the simulation box. Such systems can have a significantly smaller number of atoms, while having a similar grid size. This would lead to the LJ+PC method being significantly faster than the other two. The relaxation of the PP, which scales as $O(m)$, typically takes a negligible share (<5%) of the total simulation time, which is dominated by the force-field generation.

To clearly demonstrate the speedup achieved with GPU (OpenCL) and CPU (OpenMP) parallelization, we also compare the time required to build the FDBM force field on different platforms (see Fig. 7b): a CPU (Intel i9-13900K) using a varying number of threads, a laptop GPU (Nvidia GTX 1650Ti Mobile), a desktop GPU (AMD RX 6700 XT), and a server GPU (Nvidia A100). The measured performance profiles

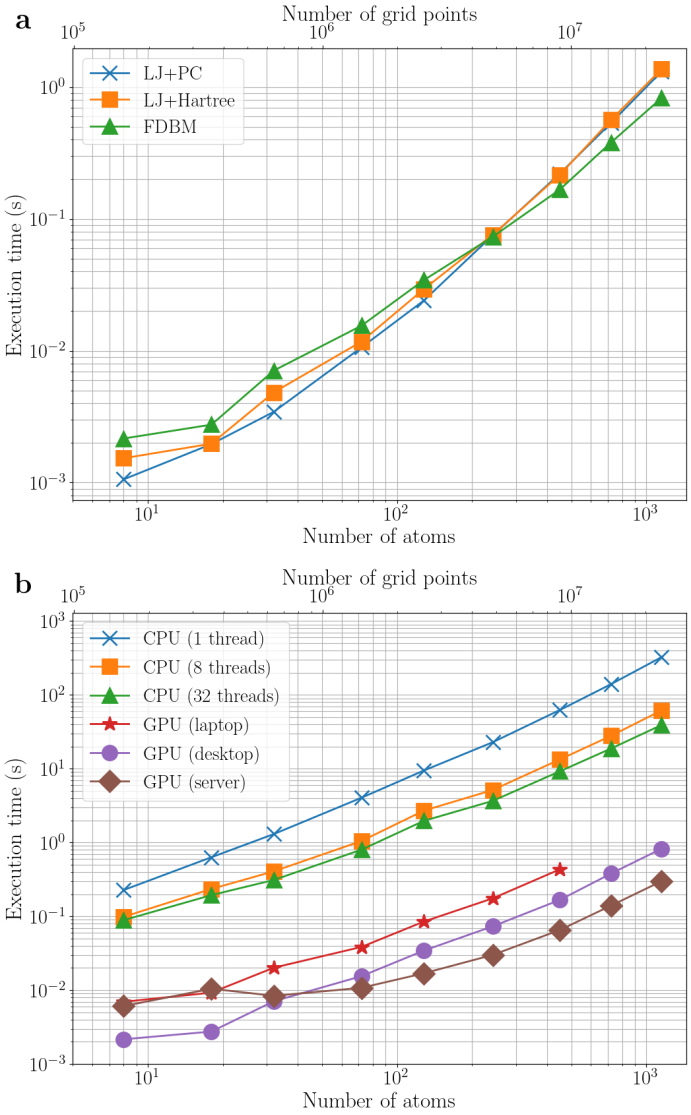

Figure 7: **Examples of performance scaling of the PPAFM code on various hardware**. Results shown in both plots (a, b) were measured for simulation of box containing periodic graphene sheet of different sizes and thus number of atoms. Notice that the number of computational grid points is proportional to the number of atoms, which allows us to plot the results with common x-axis, in this example. (a) Total the execution time (i.e. both force-field generation and relaxation) of GPU accelerated simulation, for three different levels of theory depending on the size of the system: Lennard-Jones potential with point-charges electrostatics (LJ + PC), Lennard-Jones potential + electrostatics from the Hartree potential (LJ+Hartree) and the full density based method (FDBM). These calculations were proceeded on AMD RX 6700 XT GPU. (b) Comparison of the force-field generation step for FDBM method using OpenMP acceleration with multi-core CPU and various GPUs with OpenCL. The used CPU is Intel i9-13900K, and the GPUs are: laptop Nvidia GTX 1650Ti Mobile, desktop AMD RX 6700 XT and server Nvidia A100. The last two points for the laptop GPU are missing because the memory requirement exceeds the capability of the GPU.

demonstrate that the OpenCL implementation even on the laptop GPU outperforms a single-core CPU by roughly two orders of magnitude over the whole range of sizes. The exceptions are the largest systems which do not fit into the laptop GPU memory. The server GPU is by yet another order of magnitude faster, except smallest sizes where the performance is limited by initialization overheads in the server environment. Notice that the CPU performance for 32 threads is not proportionally improved in comparison to 8 threads. This is because the CPU code uses NumPy's implementation of FFT, which is not affected by OpenMP settings. Replacing the NumPy FFT by a different better-parallelized FFT library is a simple way how to further improve performance on CPU in the future.

These measurements exclude additional time taken by loading the input files from disk and preparing arrays in the GPU memory, which actually become the bottleneck for single small simulations. However, these operations are amortized if a batch of simulations is run using the same grid, as is the case for example in the GUI when changing simulation parameters not related to the grid size.

6. Summary and conclusions

In this paper, we summarize the significant development that probe-particle model has gone through during its roughly decade-long history since its inception [5], and illustrate its computational efficiency together with its versatility through wide variety of applications in the field of high-resolution scanning probe microscopy. The sub-molecular AFM simulations model, compiled into the PPAFM package, integrates different levels of theory, described in section 2.2, allowing to balance speed and accuracy and analyze the effect of different physical interactions on resulting AFM image. Even the most accurate method implemented (FDBM) cannot exactly reproduce all physical interactions between the tip and the sample (such as deformation of electron clouds and displacement of sample atoms), which can be captured by expensive quantum mechanics calculations like DFT. Nevertheless, as demonstrated by Fig. 2 it can typically match all relevant features extremely well at a tiny fraction of the computational cost. This efficiency and the user-friendly interface, through the command-line or the GUI, makes PPAFM an ideal tool for quickly searching over different sample structures often used for sample structure recovery. The unparalleled numerical performance of PPAFM (especially in its GPU-accelerated version) has been recently exploited for the production of large databases of simulated AFM data for training machine-learned models for the reconstruction of molecular geometries from AFM images. In this area we expect great application potential, as it opens door to widespread use of high-resolution SPM methods as tool for routine single-molecule analysis.

Acknowledgements

O. K. wants to thank to Adam S. Foster and Patrick Rinke for discussions and support. N. O. has been supported by the World Premier International Research Center Initiative (WPI), MEXT, Japan and by the Academy of Finland (Projects No. 347319, 347611, 346824). A. V. Y. acknowledges the NCCR MARVEL funded by the Swiss National Science Foundation (grant No. 205602). A. G. acknowledges the financial support from the "Juan de la Cierva" fellowship (JDC2022-048249-I). P. H. gratefully acknowledges the financial support by the Czech Science Foundation Junior Star project 22-06008M. O. K. has been supported by the European Union's Horizon 2020 research and innovation programme under the Marie Skłodowska-Curie grant agreement No. 845060. The authors gratefully acknowledge Czech computer infrastructure Metacentrum, CSC – IT Center for Science, Finland, and the Aalto Science-IT project for the generous computational resources. Metacentrum resources are provided by the e-INFRA CZ project (ID:90254), supported by the Ministry of Education, Youth and Sports of the Czech Republic.

Data availability

All the data and computational procedures for obtaining the simulated images presented in this paper can be found in [64].

References

[1] G. Binnig et al. "Tunneling through a controllable vacuum gap". In: *Applied Physics Letters* 40.2 (1982), pp. 178–180. DOI: 10.1063/1.92999.

[2] G. Binnig, C. F. Quate, and Ch. Gerber. "Atomic Force Microscope". In: *Physical Review Letters* 56.9 (1986), pp. 930–933. DOI: 10.1103/physrevlett.56.930.

[3] Leo Gross et al. "The Chemical Structure of a Molecule Resolved by Atomic Force Microscopy". In: *Science* 325.5944 (2009), pp. 1110–1114. DOI: 10.1126/science.1176210.

[4] R Temirov et al. "A novel method achieving ultra-high geometrical resolution in scanning tunnelling microscopy". In: *New Journal of Physics* 10.5 (2008), p. 053012. DOI: 10.1088/1367-2630/10/5/053012.

[5] Prokop Hapala et al. "Mechanism of high-resolution STM/AFM imaging with functionalized tips". In: *Physical Review B* 90.8 (2014), p. 085421. DOI: 10.1103/PhysRevB.90.085421.

[6] Ondrej Krejčí et al. "Principles and simulations of high-resolution STM imaging with a flexible tip apex". en. In: *Physical Review B* 95.4 (2017), p. 045407. DOI: 10.1103/PhysRevB.95.045407.

[7] Prokop Hapala et al. "Origin of High-Resolution IETS-STM Images of Organic Molecules with Functionalized Tips". In: *Physical Review Letters* 113.22 (2014), p. 226101. DOI: 10.1103/PhysRevLett.113.226101.

[8] Leo Gross et al. "Bond-Order Discrimination by Atomic Force Microscopy". In: *Science* 337.6100 (2012), pp. 1326–1329. DOI: 10.1126/science.1225621.

[9] Joost van der Lit et al. "Submolecular Resolution Imaging of Molecules by Atomic Force Microscopy: The Influence of the Electrostatic Force". In: *Physical Review Letters* 116.9 (2016), p. 096102. DOI: 10.1103/PhysRevLett.116.096102.

[10] Bruno de la Torre et al. "Non-covalent control of spin-state in metal-organic complex by positioning on N-doped graphene". In: *Nature Communications* 9.1 (2018), p. 2831. DOI: 10.1038/s41467-018-05163-y.

[11] Philipp Leinen et al. "Autonomous robotic nanofabrication with reinforcement learning". In: *Science Advances* 6.36 (2020). DOI: 10.1126/sciadv.abb6987.

[12] Bruno Schuler et al. “Unraveling the Molecular Structures of Asphaltenes by Atomic Force Microscopy”. In: *Journal of the American Chemical Society* 137.31 (2015), pp. 9870–9876. DOI: 10.1021/jacs.5b04056.

[13] Shadi Fatayer et al. “Direct Visualization of Individual Aromatic Compound Structures in Low Molecular Weight Marine Dissolved Organic Carbon”. In: *Geophysical Research Letters* 45.11 (2018), pp. 5590–5598. DOI: 10.1029/2018gl077457.

[14] Katharina Kaiser et al. “Visualization and identification of single meteoritic organic molecules by atomic force microscopy”. In: *Meteoritics &amp Planetary Science* 57.3 (2022), pp. 644–656. DOI: 10.1111/maps.13784.

[15] Jonas Heggemann et al. “Differences in Molecular Adsorption Emanating from the (2 × 1) Reconstruction of Calcite(104)”. In: *The Journal of Physical Chemistry Letters* 14.7 (2023). PMID: 36794827, pp. 1983–1989. DOI: 10.1021/acs.jpclett.2c03243.

[16] Alexander Liebig et al. “Quantifying the evolution of atomic interaction of a complex surface with a functionalized atomic force microscopy tip”. In: *Scientific Reports* 10.1 (2020). DOI: 10.1038/s41598-020-71077-9.

[17] Benjamin Alldritt et al. “Automated tip functionalization via machine learning in scanning probe microscopy”. In: *Computer Physics Communications* 273 (2022), p. 108258. DOI: 10.1016/j.cpc.2021.108258.

[18] Fangzhou Xia and Kamal Youcef-Toumi. “Review: Advanced Atomic Force Microscopy Modes for Biomedical Research”. In: *Biosensors* 12 (12 2022), p. 1116. DOI: 10.3390/bios12121116.

[19] Romain Amyot, Noriyuki Kodera, and Holger Flechsig. “BioAFMviewer software for simulation atomic force microscopy of molecular structures and conformational dynamics”. In: *Journal of Structural Biology: X* 7 (2023). This is an open access article under the CC BY-NC-ND license (http://creativecommons.org/licenses/by-nc-nd/4.0/)., p. 100086. DOI: 10.1016/j.yjsbx.2023.100086.

[20] J. López-Alonso, M. Eroles, S. Janel, et al. “PyFMLab: Open-source software for atomic force microscopy microrheology data analysis”. In: *Open Res Europe* 3 (2023). Peer-reviewed version 1 with reservations., p. 187. DOI: 10.12688/openreseurope.16550.1.

[21] Benjamin Alldritt et al. “Automated structure discovery in atomic force microscopy”. In: *Science Advances* 6.9 (2020), eaay6913. DOI: 10.1126/sciadv.aay6913.

[22] Jaime Carracedo-Cosme et al. “Molecular Identification from AFM Images Using the IUPAC Nomenclature and Attribute Multimodal Recurrent Neural Networks”. In: *ACS Applied Materials & Interfaces* 15.18 (2023), pp. 22692–22704. DOI: 10.1021/acsami.3c01550.

[23] Binze Tang et al. “Machine learning-aided atomic structure identification of interfacial ionic hydrates from AFM images”. In: *National Science Review* 10.7 (2022). DOI: 10.1093/nsr/nwac282.

[24] Jaime Carracedo-Cosme et al. “QUAM-AFM: A Free Database for Molecular Identification by Atomic Force Microscopy”. In: *Journal of Chemical Information and Modeling* 62.5 (2022), pp. 1214–1223. DOI: 10.1021/acs.jcim.1c01323.

[25] Michael Ellner et al. “The Electric Field of CO Tips and Its Relevance for Atomic Force Microscopy”. In: *Nano Letters* 16.3 (2016), pp. 1974–1980. DOI: 10.1021/acs.nanolett.5b05251.

[26] A. M. Sweetman et al. “Mapping the force field of a hydrogen-bonded assembly”. In: *Nature Communications* 5.1 (2014). DOI: 10.1038/ncomms4931.

[27] Alfred John Weymouth, Thomas Hofmann, and Franz J. Giessibl. “Quantifying Molecular Stiffness and Interaction with Lateral Force Microscopy”. In: *Science* 343.6175 (2014), pp. 1120–1122. DOI: 10.1126/science.1249502.

[28] F. J. Giessibl. “A direct method to calculate tip–sample forces from frequency shifts in frequency-modulation atomic force microscopy”. In: *Applied Physics Letters* 78.1 (2001), pp. 123–125. DOI: 10.1063/1.1335546.

[29] William L. Jorgensen and Julian Tirado-Rives. “The OPLS [optimized potentials for liquid simulations] potential functions for proteins, energy minimizations for crystals of cyclic peptides and crambin”. In: *Journal of the American Chemical Society.* 110.6 (1988), pp. 1657–1666. DOI: 10.1021/ja00214a001.

[30] P. Hapala et al. “Simultaneous nc-AFM/STM Measurements with Atomic Resolution”. In: *Noncontact Atomic Force Microscopy: Volume 3*. Springer International Publishing, 2015. Chap. Simultaneo, pp. 29–49. DOI: 10.1007/978-3-319-15588-3_3.

[31] Prokop Hapala et al. “Mapping the electrostatic force field of single molecules from high-resolution scanning probe images”. In: *Nature Communications* 7.1 (2016). DOI: 10.1038/ncomms11560.

[32] Jinbo Peng et al. “Weakly perturbative imaging of interfacial water with submolecular resolution by atomic force microscopy”. In: *Nature Communications* 9.1 (2018), p. 122. DOI: 10.1038/s41467-017-02635-5.

[33] Jinbo Peng et al. “The effect of hydration number on the interfacial transport of sodium ions”. In: *Nature* 557.7707 (2018), pp. 701–705. DOI: 10.1038/s41586-018-0122-2.

[34] Prokop and Hapala. *ppafm web interface*. http://ppr.fzu.cz/. 2023.

[35] Bruno De La Torre et al. “Submolecular Resolution by Variation of the Inelastic Electron Tunneling Spectroscopy Amplitude and its Relation to the AFM/STM Signal”. In: *Physical Review Letters* 119.16 (2017), pp. 1–6. DOI: 10.1103/PhysRevLett.119.166001.

[36] Marco Di Giovannantonio et al. “On-Surface Synthesis of Indenofluorene Polymers by Oxidative Five-Membered Ring Formation”. In: *Journal of the American Chemical Society* 140.10 (2018), pp. 3532–3536. DOI: 10.1021/jacs.8b00587.

[37] Michael Ellner, Pablo Pou, and Rubén Pérez. “Molecular Identification, Bond Order Discrimination, and Apparent Intermolecular Features in Atomic Force Microscopy Studied with a Charge Density Based Method”. In: *ACS Nano* 13.1 (2019), pp. 786–795. DOI: 10.1021/acsnano.8b08209.

[38] Stefan Grimme et al. “A consistent and accurate ab initio parametrization of density functional dispersion correction (DFT-D) for the 94 elements H-Pu”. In: *The Journal of Chemical Physics* 132.15 (2010), p. 154104. DOI: 10.1063/1.3382344.

[39] Erin R. Johnson and Axel D. Becke. “A post-Hartree-Fock model of intermolecular interactions: Inclusion of higher-order corrections”. In: *The Journal of Chemical Physics* 124.17 (2006), p. 174104. DOI: 10.1063/1.2190220.

[40] Volker Blum et al. “Ab initio molecular simulations with numeric atom-centered orbitals”. In: *Computer Physics Communications* 180.11 (2009), pp. 2175–2196. DOI: https://doi.org/10.1016/j.cpc.2009.06.022.

[41] Thomas D. Kühne et al. “CP2K: An electronic structure and molecular dynamics software package - Quickstep: Efficient and accurate electronic structure calculations”. In: *The Journal of Chemical Physics* 152.19 (2020), p. 194103. DOI: 10.1063/5.0007045.

[42] Percy Zahl et al. “Hydrogen bonded trimesic acid networks on Cu(111) reveal how basic chemical properties are imprinted in HR-AFM images”. In: *Nanoscale* 13.44 (2021), 18473–18482. DOI: 10.1039/d1nr04471k.

[43] Nikolaj Moll et al. “Image Distortions of a Partially Fluorinated Hydrocarbon Molecule in Atomic Force Microscopy with Carbon Monoxide Terminated Tips”. In: *Nano Letters* 14.11 (2014), pp. 6127–6131. DOI: 10.1021/nl502113z.

[44] B. Mallada et al. “Visualization of -hole in molecules by means of Kelvin probe force microscopy”. In: *Nature Communications* 14.1 (2023). DOI: 10.1038/s41467-023-40593-3.

[45] Nikolaj Moll et al. “A simple model of molecular imaging with noncontact atomic force microscopy”. In: *New Journal of Physics* 14.8 (2012), p. 083023. DOI: 10.1088/1367-2630/14/8/083023.

[46] Dimas G. de Oteyza et al. “Direct Imaging of Covalent Bond Structure in Single-Molecule Chemical Reactions”. In: *Science* 340.6139 (2013), 1434–1437. DOI: 10.1126/science.1238187.

[47] M. Neu et al. “Image correction for atomic force microscopy images with functionalized tips”. In: *Phys. Rev. B* 89 (20 2014), p. 205407. DOI: 10.1103/PhysRevB.89.205407.

[48] Peter Liljeroth, Jascha Repp, and Gerhard Meyer. “Current-Induced Hydrogen Tautomerization and Conductance Switching of Naphthalocyanine Molecules”. In: *Science* 317.5842 (2007), 1203–1206. DOI: 10.1126/science.1144366.

[49] Fabian Mohn et al. “Imaging the charge distribution within a single molecule”. In: *Nature Nanotechnology* 7.4 (2012), pp. 227–231. DOI: 10.1038/nnano.2012.20.

[50] Pengcheng Chen et al. “Observation of electron orbital signatures of single atoms within metal-phthalocyanines using atomic force microscopy”. In: *Nat. Commun.* 14.1 (2023), p. 1460. DOI: 10.1038/s41467-023-37023-9.

[51] Jiří Doležal et al. “Real Space Visualization of Entangled Excitonic States in Charged Molecular Assemblies”. In: *ACS Nano* 16.1 (2021), 1082–1088. DOI: 10.1021/acsnano.1c08816.

[52] F. Albrecht et al. “Probing Charges on the Atomic Scale by Means of Atomic Force Microscopy”. In: *Physical Review Letters* 115.7 (2015). DOI: 10.1103/physrevlett.115.076101.

[53] Bruno Schuler et al. “Contrast Formation in Kelvin Probe Force Microscopy of Single -Conjugated Molecules”. In: *Nano Letters* 14.6 (2014), pp. 3342–3346. DOI: 10.1021/nl500805x.

[54] B. Mallada et al. “Real-space imaging of anisotropic charge of -hole by means of Kelvin probe force microscopy”. In: *Science* 374.6569 (2021), pp. 863–867. DOI: 10.1126/science.abk1479.

[55] Ondřej Krejčí et al. *PPSTM*. https://github.com/Probe-Particle/PPSTM. 2023.

[56] C. Julian Chen. “Tunneling matrix elements in three-dimensional space: The derivative rule and the sum rule”. In: *Physical Review B* 42 (14 1990), pp. 8841–8857. DOI: 10.1103/PhysRevB.42.8841.

[57] Daniel J. Rizzo et al. “Topological band engineering of graphene nanoribbons”. In: *Nature* 560.7717 (2018), pp. 204–208. DOI: 10.1038/s41586-018-0376-8.

[58] James Lawrence et al. “Combining high-resolution scanning tunnelling microscopy and first-principles simulations to identify halogen bonding”. In: *Nature Communications* 11.1 (2020). DOI: 10.1038/s41467-020-15898-2.

[59] Chi lun Chiang et al. “Real-space imaging of molecular structure and chemical bonding by single-molecule inelastic tunneling probe”. In: *Science* 344.6186 (2014), pp. 885–888. DOI: 10.1126/science.1253405.

[60] Prokop Hapala et al. *ppafm*. https://github.com/Probe-Particle/ppafm. 2023.

[61] Erik Bitzek et al. “Structural Relaxation Made Simple”. In: *Physical Review Letters* 97.17 (2006). DOI: 10.1103/physrevlett.97.170201.

[62] Charles R. Harris et al. “Array programming with NumPy”. In: *Nature* 585.7825 (2020), pp. 357–362. DOI: 10.1038/s41586-020-2649-2.

[63] Bogdan Opanchuk. *Reikna*. https://github.com/fjarri/reikna. 2023.

[64] Martin Ondráček et al. *Datasets for the paper ”Advancing Scanning Probe Microscopy Simulations: A Decade of Development in Probe-Particle Models”*. 2024. DOI: 10.5281/zenodo.10563098.